Case Studies in Thermal Engineering 50 (2023) 103477

Contents lists available at ScienceDirect

Case Studies in Thermal Engineering

journal homepage: www.elsevier.com/locate/csite

Influence of recoil pressure, mushy zone flow resistance and reflectivity on melt pool shape in laser powder bed fusion simulation

Jun Katagiri *, Masahiro Kusano, Sukeharu Nomoto, Makoto Watanabe

Additive Manufacturing Group, Research Center for Structural Materials, National Institute for Materials Science, Sengen 1-2-1, Tsukuba, 305-0047, Ibaraki, Japan

ARTICLE INFO

Keywords:
Laser powder bed fusion
Multi-physics CFD simulation
Recoil pressure
Mushy zone flow resistance
Fresnel laser reflection model
Melt pool shape

ABSTRACT

Melt pool dimensions (depth: D and width: W) are strongly correlated with defects generated in laser powder bed fusion. The melt pool dimensions have been evaluated by CFD simulation including solid–liquid–gas phase change and laser multiple reflection. Such a multi-physics simulation requires a large number of parameters. Preliminary simulations for parameter identification require a lot of time and effort. The parameter sensitivity to the melt pool dimensions is important; however, the systematic evaluations have hardly been found in the literature. In this study, we performed systematic parametric evaluation for three parameters related to recoil pressure, flow resistance in solid–liquid mushy zone and Fresnel laser reflection. As a result, the D values increased with increasing recoil pressure, but the W values did not. The flow resistance force influenced the velocities in the mushy zone but not the melt pool dimensions. The D increased with increasing reflectivity, but the W did not. The melt pool dimensions varying recoil pressure, flow resistance force and reflectivity were all inconsistent with the experimental melt pool dimensions. In order to agree with the experimental melt pool dimensions, the problems to be solved were discussed by comparing the previous studies.

1. Introduction

Laser powder bed fusion (L-PBF) is one of the most promising additive manufacturing processes. First, a thin layer of metal powder is applied to a substrate. A laser moves horizontally and then selectively melts and solidifies the powder bed to produce a sliced object derived from an arbitrarily shaped three-dimensional object. A three-dimensional part can be produced by repeating the unit process. An advantage of the L-PBF process is that it can produce complex-shaped objects that cannot be produced by conventional metal processing. However, several types of defects occur during L-PBF fabrication, depending on the laser power and laser scanning speed (the laser processing parameters) [1,2].

To identify the laser process parameter that causes the defects, a number of single-track experiments have been carried out, e.g. [2,3]. Additionally, multi-physics Computational Fluid Dynamics (CFD) simulations have been used in previous studies to evaluate the melt pool shape. Such simulations implement multiple physical phenomena such as heat conduction, fluid dynamics, solid–liquid–gas phase change are coupled. The multi-physics simulation has been successfully modelled keyhole-type defect [4], lack-of-fusion type defect during multi-track simulation [5], and balling defect [6]. Some previous studies have reported that the melt pool dimensions obtained from the simulation are in good agreement with those obtained from the experimental measurement [7,8].

The multi-physics simulation of the L-PBF process requires various physical models such as recoil pressure due to evaporation [8–10], flow resistance force in solid–liquid coexisting (mushy) zone [11], and Fresnel laser reflection model [12]. Such models include

* Corresponding author.
E-mail address: KATAGIRI.Jun@nims.go.jp (J. Katagiri).

https://doi.org/10.1016/j.csite.2023.103477
Received 28 April 2023; Received in revised form 31 August 2023; Accepted 7 September 2023
Available online 11 September 2023

parameters to be determined. These parameter values have sometimes been determined empirically. The recoil pressure and the flow resistance force are included in the conservation of momentum equation. Therefore, the values of the parameters affect the velocity of the molten metal; in other words, the parameter values will affect the melt pool shape. In addition, the previous experimental studies have shown that the laser process parameters extremely influence the melt pool shape [2], which implies an importance of the other laser properties such as the laser reflectivity. In this study, the laser multiple reflection is simulated using the ray-tracing method. The laser reflectivity in ray-tracing is calculated using the Fresnel model proposed by Cho and Na [12]. The model also includes an empirical parameter. Li et al. have evaluated the effect of the flow resistance force parameter in the mushy zone using the multi-physics simulation [13]. They reported that the mushy zone constant influenced the velocity fields inside the melt pool and the surface shape of the top of the melt pool. Alphonso et al. have performed the multi-physics simulations with and without recoil pressure [14] and reported that the melt pool depth obtained from the simulation with recoil pressure was greater than that without recoil pressure. Despite the importance of the three parameters for the melt pool shape, i.e., the defects to be formed, there is little systematic evaluation of the parameters in the literature. The users of the L-PBF machine should choose the material to be used, the powder properties, the part design, the process parameters and so on. To find the optimum processing parameters for L-PBF, a series of preliminary experiments varying the process parameters requires a lot of time and money. Computer simulation should be an extremely powerful tool; such a virtual testing tool enables us to efficiently optimise the processing parameters of L-PBF.

In this study, three case studies were carried out to evaluate the effect of recoil pressure, mushy zone flow resistance force and laser reflectivity on the melt pool dimensions. In addition, the single-track experiments were also carried out. The simulation methodology, including its governing equations and the physical models used, and the single-track experiment are briefly summarised in Section 2. In Section 3, a series of simulations were carried out to vary the three parameters. We found that the recoil pressure and the reflectivity parameters affected the melt pool depth, while the flow resistance force parameter did not. The Fresnel reflection model parameter was the most influential parameter on the melt pool depth among the three parameters. All the three parameters hardly influenced the melt pool width. Although the three parameters varied significantly, the melt pool dimensions obtained from the simulations did not agree with those obtained from the single-track experiments. The reason for this discrepancy was then discussed. Finally, the conclusions of this study and the problems to be solved for simulating the melt pool dimensions obtained from the experimental measurement are described in Section 4.

2. Materials and methods

2.1. Discrete element modelling of powder bed formation

The powder bed formed on the substrate is modelled using the Discrete Element Method (DEM) [15]. The DEM is used to simulate frictional rigid particle assemblies. We used the LIGGGHTS (version 3.8.0) to generate the powder bed. More than 80% by volume of the powders used in single-track experiment as described below were between 20 μm and 40 μm in particle diameter, with an average diameter of 28.9 μm. To model the particle size distribution, the spherical particles, whose diameter ranged between 20 μm and 40 μm and average diameter was 27.5 μm, were used in the DEM simulation.

The Hertz contact model was used in the simulation and its stiffness (Young's modulus) and Poisson's ratio were set to 1.3×10^{11} N/m and 0.33, respectively. The particle damping coefficient was set to be 0.5 of the particle restitution coefficient. The friction coefficients of particle–particle contact and particle–wall contact were both 0.1. The boundary conditions for the six side faces were set to the f boundary style implemented in LIGGGHTS. The f style boundary basically acts as a fixed smoothed wall boundary, but the particles are lost if the particle position is outside the domain.

The overview of the powder bed formation simulation is as follows. First, the particles were generated to a rectangular area above the powder bed to be formed. The particles were deposited under gravity on the powder bed stage, whose width and length are 1.0 mm and 0.5 mm respectively. An initial height of the powder bed stage is 0.03 mm. After the gravitational deposition, a rigid rectangular wall moves in the y direction for 1.0 mm to remove the particles whose height is higher than 0.03 mm.

To incorporate the formed powder bed into the multi-physics CFD simulation, a stereolithography (STL) was generated using the positions and radii of all particles obtained from the DEM simulation. The powder particles are therefore fixed, which means that the particle packing structure does not change during the simulation described below.

2.2. Governing equations and physical models

The simulation solvers are based on a general purpose CFD software of OpenFOAM (version 8) and partly customised for modelling the L-PBF: *TBinterFoam* solver (TERRABYTE Co., Ltd., Tokyo, Japan). The short summary of the *TBinterFoam* solver is described in this section.

The governing equations of conservation of energy, conservation of mass and conservation of momentum are expressed by Eqs. (1)–(3) respectively.

$$\frac{\partial(\rho C_p T)}{\partial t} + \frac{\partial(\rho u_j C_p T)}{\partial x_j} = -\frac{\partial q_j}{\partial x_j} + \dot{q_m} + \dot{q_v}, \tag{1}$$

$$\frac{\partial u_i}{\partial x_i} = 0, \tag{2}$$

$$\frac{\partial(\rho u_i)}{\partial t} + \frac{\partial(\rho u_i u_j)}{\partial x_i} = -g_j\left(x_j - r_j\right)\frac{\partial \rho}{\partial x_i} + \frac{\partial}{\partial x_j}\left\{\mu\left(\frac{\partial u_i}{\partial x_j} + \frac{\partial u_j}{\partial x_i}\right)\right\} + F_{CSF,i} + F_{r,i} + S_i, \tag{3}$$

where ρ, C_p, u_i, r_j, q_j, μ, $\dot{q_m}$ and $\dot{q_v}$ are the density, specific heat capacity, flow velocity, reference point, heat flux, viscosity, phase change heat dissipation term and phase change heat absorption term, respectively. Eqs. (1)–(3) were solved by the finite volume method (FVM) in OpenFOAM. FVM is one of the most widely used methods for computational fluid dynamics (CFD) simulation. A computational domain is partitioned by a set of polyhedral volume elements called control volumes. The governing equations (partial differential equations) are discretised to algebraic equations. The discretised equations are conservative for each control volume. The FVM and OpenFOAM software are described in detail in the references cited [16–19].

The term $F_{\mathrm{CSF},i}$ is the surface tension term using continuum surface force (CSF) model which is expressed as follows.

$$F_{CSF,i} = \sigma\kappa\frac{\partial F}{\partial x_i}, \tag{4}$$

where σ and κ are the surface tension coefficient and the curvature of the gas–liquid interface, respectively. Note that the interface of solid or metal (phase 1) and gas (phase 2) is captured by the function F using the Volume-of-Fluid (VOF) method , which is expressed as follows:

$$\frac{\partial F}{\partial t} + \frac{\partial F u_j}{\partial x_j} = 0. \tag{5}$$

The F is the value of the VOF function and ranges between 0 and 1. The gas–liquid interface is represented by the volume ratio of phase-1 and phase-2 and its dynamics is calculated by solving the advection equation of F.

The term $F_{\mathrm{r},i}$ in Eq. (3) is recoil pressure and is expressed by Eq. (6).

$$F_{r,i} = -\alpha P_0 \exp(\left(L_v\frac{T - T_v}{RTT_v}\right))\mathbf{n}, \tag{6}$$

where, α, P_0, L_v, R, T_v, and $\mathbf{n}$ are an arbitrary constant value, the gas phase pressure, the latent heat of evaporation, the gas constant, the evaporation temperature, and a unit normal vector of the gas-liquid interface.

The term S_i in Eq. (3) represents flow resistance force mushy zone, i.e., solid–liquid coexisting zone and is known as Voller–Prakash model [11]. The Voller–Prakash model is described by Eq. (7).

$$S_i = -C\frac{\left(1 - g_l\right)^2}{{g_l}^3}u_i, \tag{7}$$

where C and g_l are an arbitrary constant and the volume ratio of the liquid phase, respectively.

An enthalpy is calculated using Eq. (8).

$$H = g_s\int_{T_{ref}}^{T}\rho_s C_s dT \; + g_l\int_{T_{ref}}^{T}\rho_l C_l dT \; + \rho_l C_l L, \tag{8}$$

where, g_s, C_s, C_l, T_{ref}, and L are the solid fraction, i.e., g_l+g_s=1, specific heat of solid phase, specific heat of liquid phase, reference temperature, and latent heat of fusion, respectively. Assuming that the latent heat and the density are independent of the temperature, Eq. (9) is derived.

$$H = g_s\rho_s C_s T + g_l\rho_l C_l T + g_l\rho_l L. \tag{9}$$

The term $\dot{q_m}$ in Eq. (1) is expressed by following equation.

$$\dot{q_m} = -\rho_l L\frac{\partial g_l}{\partial t}. \tag{10}$$

The enthalpy considering the evaporation is expressed by Eq. (11).

$$H = g_s\int_{T_{ref}}^{T}\rho_s C_s dT \; + g_l\int_{T_{ref}}^{T}\rho_l C_l dT \; + \rho_l C_l L + g_v\int_{T_{ref}}^{T}\rho_v C_v dT + \rho_v C_v L_v, \tag{11}$$

where, g_v, C_v, ρ_v, and L_v are the gas fraction, specific heat of evaporation, gas density, and latent heat of evaporation, respectively. Assuming that the latent heat and the density are independent of the temperature, Eq. (12) is derived.

$$H = g_s\rho_s C_s T + g_l\rho_l C_l T + g_v\rho_v C_v T + g_l\rho_l L + g_v\rho_v L_v. \tag{12}$$

The term $\dot{q_v}$ in Eq. (1) is expressed by following equation.

$$\dot{q_v} = -\left(\rho_v C_v(T - T_{ref}) + \rho_v L_v\right)\frac{\partial g_v}{\partial t}. \tag{13}$$

Heat flux (q) between the metal surface and the gas phase is expressed by Eq. (14).

$$q = -h(T - T_g) - \epsilon_h\sigma_b(T^4 - {T_g}^4), \tag{14}$$

where h, T_g, ϵ_h and σ_b are the heat transfer coefficient, gas phase temperature, surface emissivity and Stefan–Boltzmann constant (5.67×10^{-8} $\mathrm{Wm^{-2}K^{-4}}$) respectively.

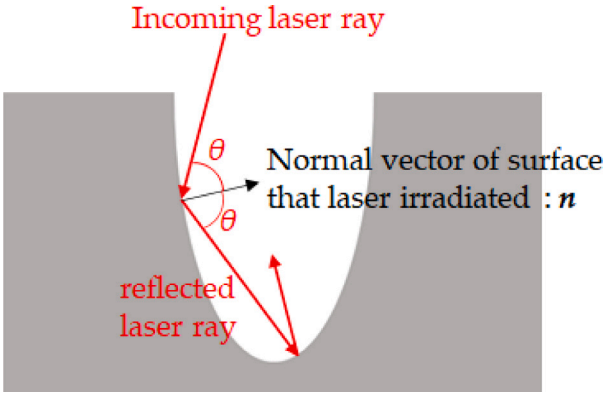

Fig. 1. A schematic of Fresnel reflection model.

Various moving heat source models have been used in the simulation of the L-PBF process, such as the application of a Gaussian heat source to the surface [8], the volumetric heat source model in which the laser energy is absorbed depending on the depth from the metal surface [20,21], and the ray tracing method [5,6]. The ray tracing method is one of the solvers used in this study. The laser beam is assumed to consist of a bundle of laser beams. The ray tracing method tracks each ray. Fig. 1 shows a schematic of the ray tracing method. When the laser reaches the metal surface, thermal energy is applied to the metal surface. The thermal energy applied has been calculated in inverse proportion to the laser reflectivity of the metal surface. The laser beam repeats the mirror reflections until (1) the applied energy became extremely small or (2) the laser beam did not reach the metal surface. The reflectivity (R_L) is calculated using the Fresnel reflection model in the ray tracing method [12].

$$R_L = \frac{1}{2}\left(\frac{1+(1-\epsilon\cos\theta)^2}{1+(1+\epsilon\cos\theta)^2} + \frac{\epsilon^2 - 2\epsilon\cos\theta + 2\cos^2\theta}{\epsilon^2 + 2\epsilon\cos\theta + 2\cos^2\theta}\right), \tag{15}$$

where, θ and ϵ are the laser incident angle and an arbitrary constant, respectively.

The laser energy distribution implemented in the *TBinterFoam* solver is a Gaussian distribution. The heat flux (q_b) which is expressed as follows.

$$q_b = C(P)\exp\left(-\frac{r^2/{r_L}^2}{2{\sigma_G}^2}\right), \tag{16}$$

where, $C(P)$, r_L, and σ_G are a scaling factor depending on the laser power (P), the laser spot radius (40×10^{-6} m in this study), and the standard deviation of the Gaussian distribution (1.0 in this study). Note that the formula for $C(P)$ is not described in the vendor's manual.

The explicit Euler time integration scheme, the linear interpolation scheme for the Laplacian and gradient discretisation, and the second-order linear upwind and total variation diminishing (TVD) schemes for the divergent discretisation were used. Note that the third-order linear upwind scheme is often used in CFD simulation. We chose the TVD scheme because the preliminary simulation using the TVD scheme was more stable compared to the third-order linear upwind scheme.

The Gauss–Seidel method was used to calculate the flow and temperature fields. The tolerance value of the flow velocity and temperature was 1.0×10^{-6}. The incomplete Cholesky preconditioned conjugate gradient method was used for the pressure calculation. Considering the balance between calculation accuracy and speed, the residual value for the iteration was 1.0×10^{-6} to ensure the stability of the calculation.

Note that the governing equations and physical models used are the same as those used in the previous studies of L-PBF simulation [3–8,14,20–23]. The dynamics of the gas phase is sometimes not considered in the previous studies; on the other hand, both the dynamics of the fluid and the gas phase are considered in this study.

2.3. Physical properties and calculation parameters used

The material used in this study is Inconel738LC which is a nickel based alloy. The material properties and simulation parameters used are listed in Table 1. Note that the material properties are based on the calculation of CALPHAD software: JMatPro (www.sentesoftware.co.uk/jmatpro (accessed 7 April 2023)).

The dynamics of the melt pool is calculated using Eq. (3). Eq. (3) includes the source terms of Eqs. (4), (6) and (7), which means that the parameters in these equations can influence the melt pool dimensions. Eq. (15) is not included in Eq. (3); however, Eq. (15) directly influences the heat flux applied to the metal. Hence, we have performed a series of parameter sensitivity analyses for the three parameters.

Table 1
Materials properties of Inconel738LC and the simulation parameters used in this study.

Property or parameter	Value [Unit]
Density of solid	8820 [kg/m^3]
Density of liquid	8220 [kg/m^3]
Density of Gas	1.176 [kg/m^3]
Solidus temperature	1371.15 [K]
Liquidus temperature	1620.15 [K]
Evaporation temperature	3034.0 [K]
Thermal conductivity	46.1 [W/(m K)]
Latent heat of fusion	25,000 [J/kg]
Latent heat of evaporation	734,000 [J/kg]
Specific heat capacity of metal	710 [J/kg K]
Specific heat capacity of gas	1007 [J/kg K]
Surface tension coefficient (σ)	1.2 [N/m]
Liquid viscosity (μ)	0.005 [Pa s]
Gas viscosity	1.865×10^{-5} [Pa s]
Liquid–gas heat transfer coefficient	40 [W/(m^2 K)]
Emissivity of thermal radiation	0.3 [–]
Laser power (P)	300 [W]
Laser scanning speed (V)	1.0 [m/s]
Laser diameter	80.0×10^{-6} [m]
Laser type	Parallel beam ray [–]
Laser energy distribution	Gaussian [–]
Standard deviation of Gaussian distribution	1.0 [–]
Value of α in Eq. (6)	0.05 - 500 [–]
Value of C in Eq. (7)	10^{-1} - 10^{9} [kg/(m^3 s)]
Value of ϵ in Eq. (15)	0.2 - 1.0 [–]

2.4. Simulation

Fig. 2(a) shows the snapshot at the start of the simulation. We used a rectangular simulation model with width, depth and height of 0.5 mm (-0.25 mm $\leq x \leq 0.25$ mm), 1 mm (0 mm $\leq y \leq 1.0$ mm) and 0.3 mm (-0.2 mm $\leq z \leq 0.1$ mm) respectively. The grid size used must affect the simulation results. We have performed preliminary simulations varying the grid size; as a result, the melt pool dimensions obtained from the simulation became almost the same when the grid size was smaller than 5 μm. Hence, hexagonal mesh with the grid size of 5 μm was used in this study. Note that the mesh size was changed to 2.5 μm for a rectangular region within the simulation model of 0.4 mm width, 0.8 mm depth and 0.15 mm height. This resulted in a total of 5760,000 cells. The past studies have used the same or similar grid size; e.g., 3 μm [5], 4 μm [4], 4.5 μm [7], and 5 μm [14].

As a typical room temperature, the initial temperatures of metal and atmosphere were set at 298.15 K. For the thermal simulation, a constant temperature of 298.15 K was applied to the top x–y plane, and an adiabatic boundary condition was applied to the other five planes. For the pressure, an atmospheric pressure (101,325 Pa) was adopted for the upper x–y plane, and a zero-gradient condition was adopted for the other five sides. For the flow velocity, the *pressureInletOutletVelocity* boundary condition implemented in OpenFOAM was adopted for the upper x–y plane. The *pressureInletOutletVelocity* condition assumed a zero gradient condition when the flow direction is outward. When the flow direction is inward, the velocity is obtained from the flow with the specified inlet direction. The zero-gradient condition was applied to the other five sides.

Figs. 2 (b) to (f) show the snapshots during the example case of the simulation for $P = 300$ W and $V = 0.9$ m/s. A starting point of the laser is indicated by white circle in Fig. 2(a). The laser irradiation direction was vertical downwards. The laser moved towards the y direction for 0.7 mm. The laser process parameters were set to $P = 300$ W and $V = 1.0$ m/s to compare with the single-track experiment as described below. When $V = 1.0$ m/s, the simulation time was 0.0007 s. The computation time for a typical case was about 60 h on a 96-core parallel computation using an Intel Xeon Platinum 8268 processor (clock speed: 2.9 GHz).

After the simulation, the temperature fields were visualised in the cross section of the centre of the model: 0.5 mm in the y direction. Isolines of solidus and liquidus temperatures were plotted on the visualised image. The dimensions of the melt pool were measured from the visualised image. The melt pool depth obtained from the simulation is defined as the length between the deepest point of the liquidus temperature isoline and the top of the substrate. Fig. 3(a) shows a schematic of the melt pool measurement for the CFD simulation and the single track experiment. The melt pool width obtained from the simulation is defined as the length between the minimum and maximum points of the liquidus temperature along the x direction. The melt pool depth and width were measured in the similar way using the melt pool visually recognised from the cross-sectional image.

The melt pool obtained from the single-track experiment forms a semicircle on the substrate, whereas that obtained from the simulation does not. The semicircle forms because the surface tension of the melt attracts the surrounding unmelted powder particles. The dynamics of the solid particles is not coupled in the present simulation; therefore the semicircle shape cannot be formed in the CFD simulation. In addition, the time history of the temperature at a measurement point shown in Fig. 3(b) was calculated from the simulation data.

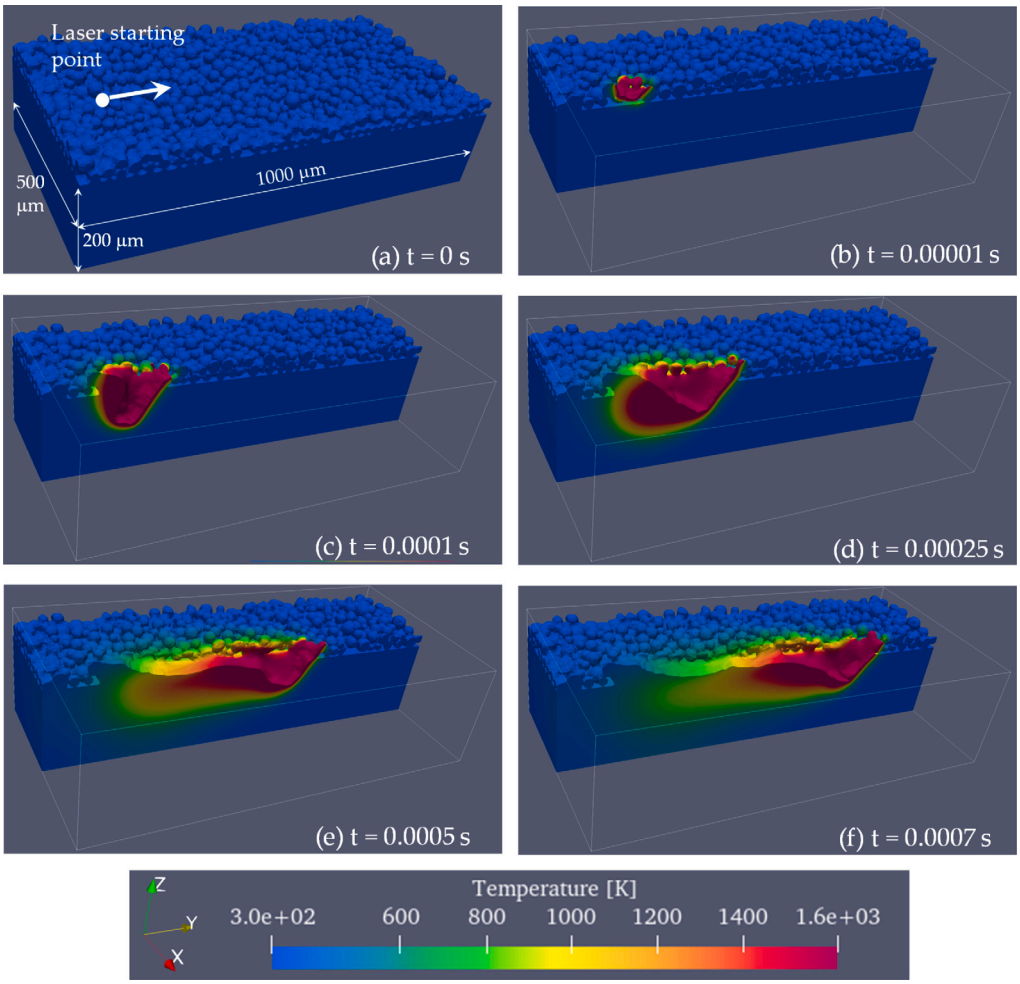

Fig. 2. Snapshots during a sample simulation for P = 300 W and V = 0.9 m/s at t = 0 s (a), 0.00001 s (b), 0.0001 s (c), 0.00025 s (d), 0.0005 s (e), and 0.0007 s (f).

2.5. Single-track experiment

A procedure for the single-track experiment has been described in detail in the cited Refs. [24]. A brief summary of the experimental procedure is described here.

The powder and substrate material used in this study was Inconel738LC. The average particle diameter was 28.9 μm. The scanning track was cut in the centre of the track line with a high precision cutting machine. Resin was embedded in the cross section and polished using a polishing machine. Note that a colloidal silica solution was added during the final polishing process. The cross section was then washed with water and allowed to dry sufficiently. The surface of the cross section was examined by scanning electron microscopy (SEM). The width and depth the melt pool was measured from the SEM image as shown in Fig. 3(a). This technique is widely used in the relevant research community to quantify the melt pool dimensions.

3. Results and discussions

3.1. Case study 1: Influence of recoil pressure

Fig. 4 shows the time evolution of the temperature for the simulations with α = 0.05, 0.5, 5, 50 and 500 respectively. The temperature becomes high as the laser source approaches the measurement point and then decreases as the laser source recedes. Such temperature trends have been observed in previous studies [5,7,22]. A maximum temperature occurred at about t = 0.0003 s and becomes low as a function of α, except for α = 0.05. The recoil pressure is the force pushing down the metal surface caused by the ejection of gas particles due to the evaporation. The metal surface is excavated by the recoil pressure. The molten metal mass arose from the excavation flows in the opposite direction to the laser movement and accumulates backwards.

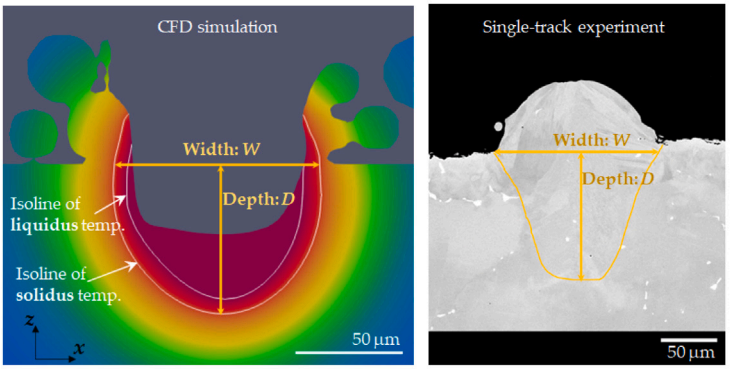

(a) A schematic of measurement of melt pool dimensions

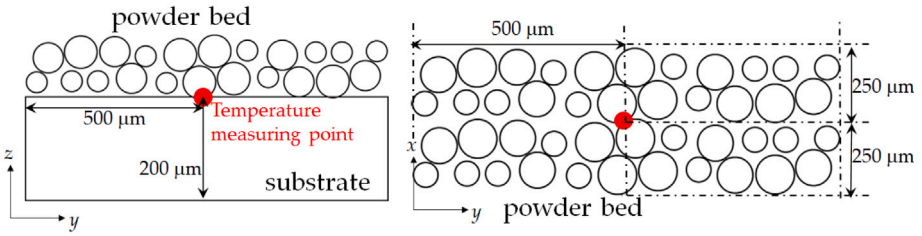

(b) A schematic of a temperature measuring point

Fig. 3. A schematic of the measurement of melt pool dimensions (a) and the temperature (b).

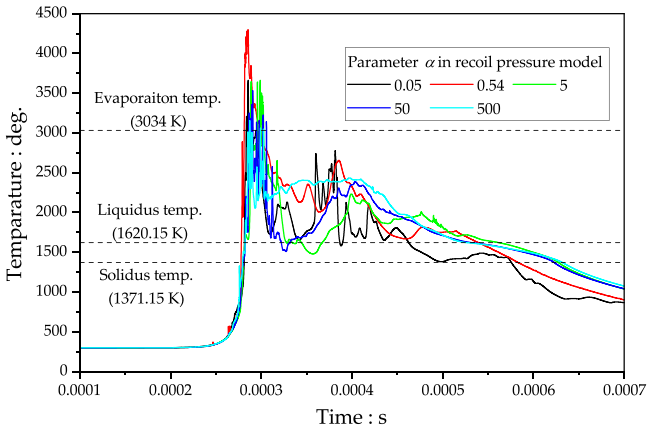

Fig. 4. Time evolution of the temperature for the simulations varying the parameter α in recoil pressure arising when the metal vaporisation (Eq. (6)).

Fig. 5 shows the metal surface profiles (isoline of VOF function value of 0.5) at $t = 0.0006$ s for $\alpha = 0.05$, 0.54, 5, 50, and 500. The excavated depth at about $y = 0.75$ mm is greater as α increases; the trend is similar to the previous study [14]. According to the study [14], the melt pool depth obtained from the simulation with recoil pressure is greater than that without recoil pressure. When α was 0.05, the metal mass hardly accumulated backwards; in other words, the powder bed and the upper part of the substrate appeared to be scraped off. The evaporated volume (mass) is converted to the recoil pressure in the CFD simulation. When the α is small, the recoil pressure is underestimated. As a result, the powder bed and the top of the substrate appeared to disappear.

The $\alpha = 0.54$ is a commonly used value in the past studies and is determined by considering the Knudsen layer during evaporation [9,10,25]. In the CFD simulation algorithm, the recoil pressure F_r is calculated on the basis of $\dot{m}_v \cdot v_T$, where $\dot{m}_v$ and v_T are the evaporated mass and the velocity at the end of the Knudsen layer [26]. Assuming that v_T is equal to the local sound velocity [9,10], Anismov [9] obtained $\alpha = 0.54$. The molten mass moved backwards and the surface height returned to the top of the substrate. When $\alpha \geq 5$, the melt accumulate+d backwards at 1.5×10^{-4} m $< y < 3.0 \times 10^{-4}$ m depending on α. However, the shape of the melt pool above the substrate often forms a semicircle or a segmented circle whose area is larger than the semicircle in the

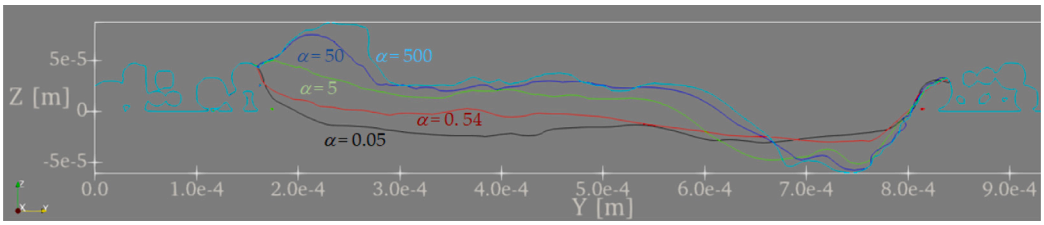

Fig. 5. The isolines of VOF function value of 0.5 at t = 0.0006 s for the recoil pressure parameter: α = 0.05 (black), 0.54 (red), 5 (light-green), 50 (blue), and 500 (light-blue). (For interpretation of the references to colour in this figure legend, the reader is referred to the web version of this article.)

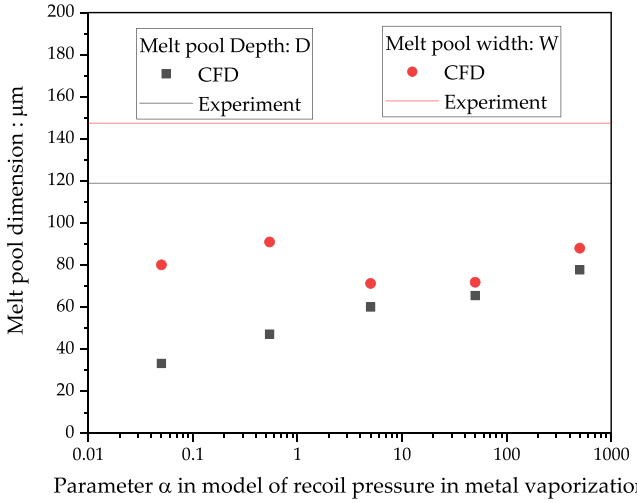

Fig. 6. Relationship between recoil pressure parameter: α in Eq. (6) and the melt pool dimension: melt pool depth D and width W obtained from the simulation and the single-track experiment under P = 300 W and V = 1.0 m/s.

single-track experiment, as shown in Fig. 3(a). The semicircle did not form in the CFD simulations because the semicircle should be formed by two mechanisms: (1) the backward accumulation and (2) the attraction of powder particles due to surface tension. During the particle melting process, the molten liquid should attract and absorb the (unmelted) powder particle by the surface tension. In contrast, the powder particles in the area near the scanned track are scattered due to the recoil pressure induced by evaporation: the spattering phenomenon [27]. The size and shape of the semicircle on the substrate should depend on the balance between the attracted and absorbed particles and the scattered particles. To reproduce the semicircular shape in the CFD simulation, the solid particle dynamics should be coupled with the CFD simulation, e.g. DEM-CFD coupling [28,29]. Note that the recent multi-physics simulations using DEM-CFD coupling [30,31] and smoothed particle hydrodynamics modelling [32] have incorporated the motion of the solid particle assembly into the multi-physics simulation of L-PBF.

Fig. 6 shows the relationship between the α and the melt pool dimension: the melt pool depth D and width W obtained from the CFD simulation and the single-track experiment. As described above, D increases with increasing α due to the surface excavation caused by the recoil pressure. On the other hand, W is around the laser spot diameter (80 μm) regardless of α. Since the laser beam direction is perpendicular downward, the surface planes near the edges of the excavated region are parallel to the laser beam direction. In such a case, the surface plane hardly absorbs the thermal energy from the laser irradiation according to the Fresnel model; as a result, the measured W values were almost equal to the laser spot diameter. However, the D and W values obtained from the simulation are different from those obtained from the single-track experiments, which indicates that the melt pool dimension in the single-track experiment can hardly be simulated just by varying α.

3.2. Case study 2: Influence of mushy zone flow resistance

Fig. 7(a) shows the time evolution of the temperature for the simulations with $C = 10^{-1}$, 10^{1}, 10^{5}, and 10^{7} respectively. As shown in the figure, the general trend of temperatures for different C is almost the same. The C is the influencing parameter of the solid–liquid coexistence region, which means that the C is valid between the solidus and liquidus temperature. The temperature range is known as brittleness temperature range (BTR). The temperature falls into the BTR at three times: t = 0.00028 s (P1), 0.00035 s (P2) and 0.00055 s $\leq t \leq$ 0.00062 s (P3). The temperatures at P1, P2 and P3 are in the solid–liquid translation phase, in the gas phase due to evaporation and in the liquid–solid solidification phase respectively. Eq. (7) is not valid for P2 because

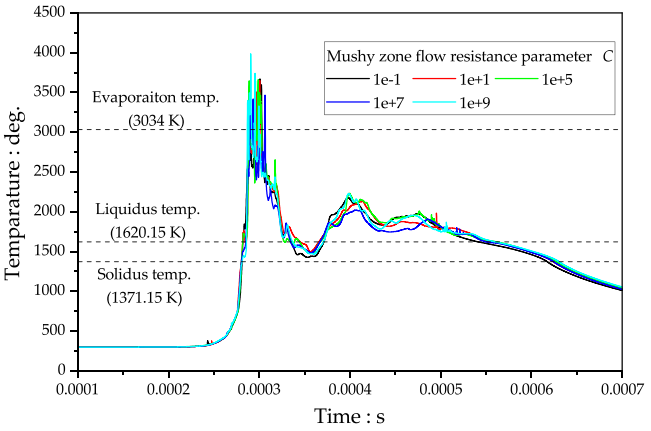

Fig. 7. Time evolution of the temperature for the simulation varying the mushy zone flow resistance parameter in Eq. (7): $C = 10^{-1}$, 10^{1}, 10^{5}, 10^{7}, and 10^{9}.

Eq. (7) is for the solid–liquid mushy zone. In the P1 state, the temperature rises rapidly for a short time. As the melting process in P1 stops for the short time, C has little effect on the temperature history. The solid–liquid mushy zone at P3 exists for a longer time compared to the P1 state.

Fig. 8 shows the velocity fields at $t = 0.0006$ s in the y–z cross section for $C = 10^{-1}$, 10^{1}, 10^{5}, 10^{7} and 10^{9}. The colour bar in the figure represents the cell velocity component of the y direction. The solid white lines in the figures show the isolines of the solidus and liquidus temperatures. The area between the two white lines is the mushy zone, so the value of C affects the velocity in this area. The molten metal mass accumulates backwards and therefore moves in the negative direction y. Note that the positive velocities, i.e. the red coloured region, occur in the mushy zone because the accumulated mass forms a convective flow. As shown in the figure, the flow velocities in the mushy zone become small as C increases.

Fig. 9 shows the effect of C on the melt pool dimensions. As shown in the figure, C has little effect on the depth and width of the melt pool. Voller and Prakash, who developed Eq. (7), proposed the reference values of C: 1.6×10^{3} and 1.6×10^{4} [11]. In the previous studies of the L-PBF simulations, the C values were 5.57×10^{6} [8], 10^{14} [6] and $10^{5}-10^{7}$ [5].

Note that the value of C cannot be varied in the experiment. The C depends on g_l; however, g_l: the volume of the fully molten metal region is extremely difficult to measure in the experiment. According to the previous study, the C value influences the surface shape and the internal velocity field of the melt pool [13]. In the present study, C varied widely between 10^{-1} and 10^{9}; however, the melt pool dimensions were almost constant regardless of C.

As discussed in [11], an applicability of the Kozeny–Carman equation should be evaluated. The correlation between C and the micro-structural parameters originally included in the Kozeny–Carman equation should be clarified. Voller and Prakash focused on a pressure drop due to porosity (i.e. liquid fraction) in the Kozeny–Carman equation and derived Eq. (7). They changed the pressure–porosity relation to a force–porosity relation by the parameter C. The Kozeny–Carman equation includes the micro-structural parameters such as the specific surface area, the hydraulic tortuosity (τ_h) which characterises the streamline length of pore throats in porous media, and the shape factor which characterises the shape of the cross-section of the porous media perpendicular to the flow direction [33]. The reference values of C can be estimated from the micro-structural parameters, but the values of the micro-structural parameters depend on other factors such as the physical phenomena being simulated. A universal reference value of C is difficult to determine, so the C values have to be determined by trial and error. The reference value of C considering the L-PBF process will be determined in our future study. Furthermore, the applicability of the Kozeny–Carman equation should be considered, as the Kozeny–Carman equation is used for the Darcy flow which is an extremely low Reynolds number flow. During the L-PBF process, the molten metal mass may become partially inertial flow. In the inertial flow regime, the porous flow is treated as a Forchheimer flow [34]. The Ergun equation [35] is a commonly used empirical equation to model the pressure–porosity relationship for Forccherimer flow. The flow resistance force using the Ergun equation should be included in the simulation and compared with that using the Kozeny–Carman equation.

3.3. Case study 3: Influence of laser reflectivity

Fig. 10 shows the relationship between a laser incident angle and the reflectivity values calculated by Eq. (15) for different values of ϵ. The reflectivity value becomes small as the ϵ value increases.

Fig. 11 shows the temperature fields in the x–z cross section at the centre of the scan track ($y = 0.5$ mm) for the simulation with $\epsilon = 0.2$, 0.6 and 1.0. The solid white lines are the solidus and liquidus temperatures respectively. The reflectivity decreases with increasing ϵ. The metal surface absorbs more thermal energy for larger ϵ; as a result, the melt pool depth becomes large as a function of ϵ.

The effect of ϵ on the melt pool dimensions is shown in Fig. 12. It is quantitatively clarified that the melt pool depth increases with increasing ϵ; however, the D obtained from the simulation differs from that obtained from the single-track experiment.

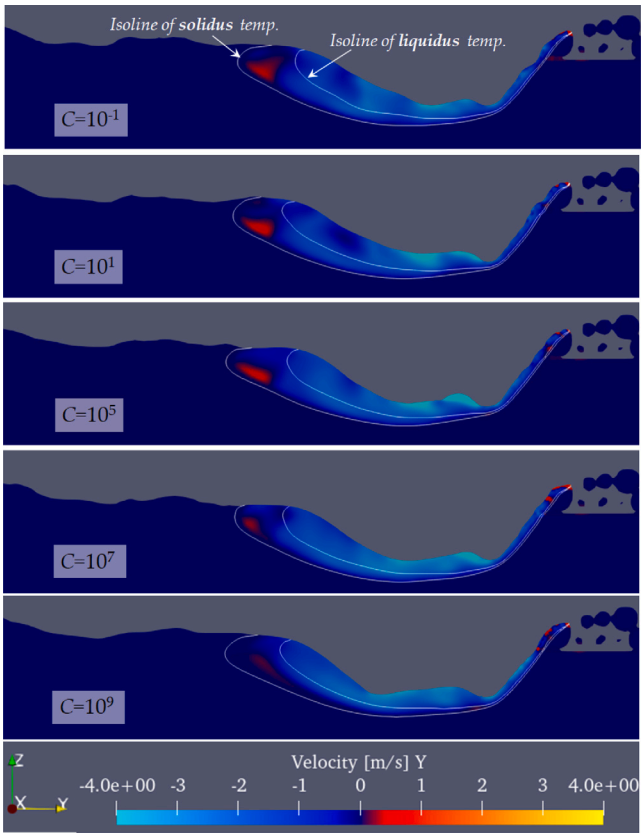

Fig. 8. Fields of the cell velocity component in y direction at t = 0.0006 s in the y–z cross-section for the mushy zone flow resistance parameter: $C = 10^{-1}$, 10^{1}, 10^{5}, 10^{7}, and 10^{9}.

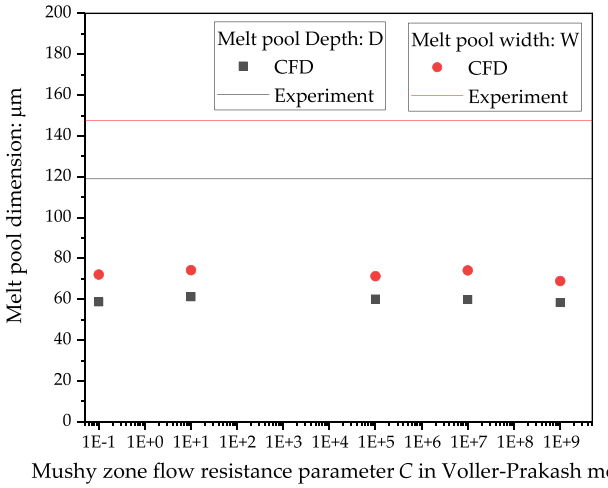

Fig. 9. Relationship between the mushy zone flow resistance parameter:C and the melt pool dimensions: melt pool depth D and width W obtained from the simulation and the single-track experiment under P = 300 W and V = 1.0 m/s.

The Fresnel model calculates the reflectivity by geometrical reflection analysis, which means that the simulation using the ray-tracing with the Fresnel model is difficult to reproduce the D in the single-track experiment. Conventional range of ϵ values is between 0.2 and 0.25. The direction of the laser irradiation is downward in the z direction. The θ was 0 degrees when the laser was irradiated in the horizontal plane; in this case the reflectivity is about 0.67 and 0.61 for ϵ of 0.2 and 0.25 respectively. According to the previous studies, the melt pool dimensions obtained from the simulations using a constant reflectivity value of 0.7 [23] and

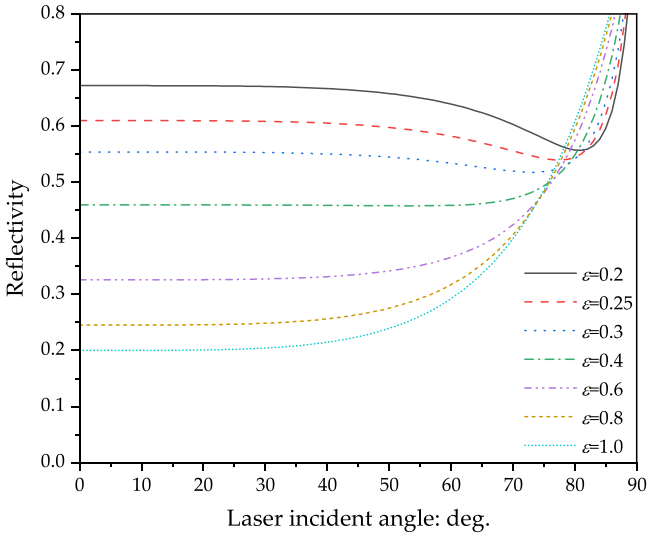

Fig. 10. Relationship between a laser incident angle and the reflectivity values calculated by Fresnel laser reflection model:Eq. (15) for different values of an empirical parameter: ϵ.

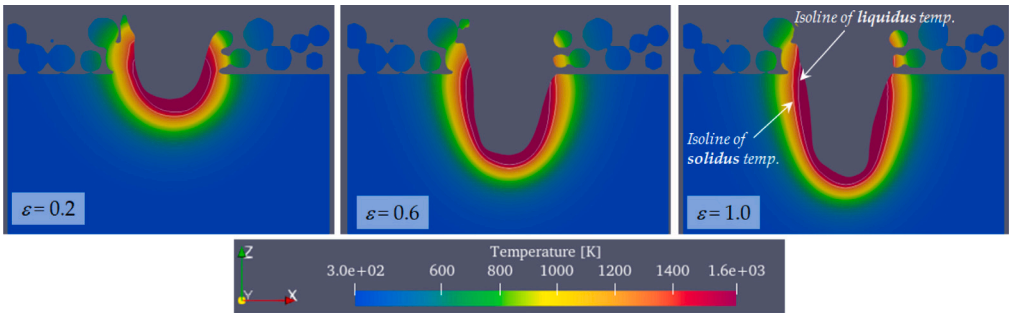

Fig. 11. Temperature fields in the x–z cross section at the centre of the scan track (y = 0.5 mm) for the simulation with the parameter in Fresnel reflection model (Eq. (15)): ϵ = 0.2, 0.6 and 1.0. The solid white lines are the solidus and liquidus temperatures respectively.

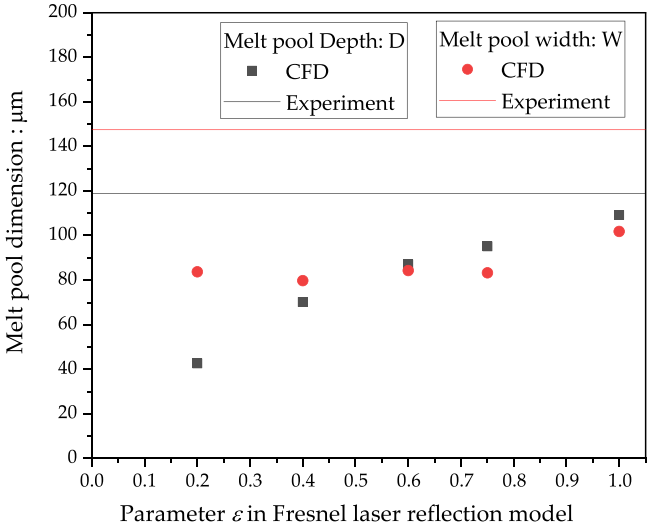

Fig. 12. Relationship between the parameter in Fresnel reflection model (Eq. (15): ϵ and the melt pool dimensions: melt pool depth D and width W obtained from the simulation and the single-track experiment at P = 300 W and V = 1.0 m/s.

0.8 [4] agreed well with those obtained from the experiments. The melt pool dimensions obtained in this study are significantly different from those obtained in the single-track experiment. The physical properties of Inconel738LC in this study are based on CALPHAD and are similar to the previous study for the same material [3], which means that the other parameters are important to simulate the melt pool dimensions. One possibility is the shape of the Gaussian distribution. The following form of Gaussian distribution has been used in the field of laser technology and has been used in the L-PBF simulations in numerous studies in the past, e.g. [3,5–8].

$$q_b = \frac{2PA}{\pi {r_L}^2} \exp\left(-2\frac{r^2}{{r_L}^2}\right), \tag{17}$$

where A is the absorptivity. Since the transmissivity of metal is zero, $A = 1 - \tau$. The q_b is linearly correlated with A in Eq. (17). The thermal energy applied to the metal surface varies as a function of A, which implies that the laser reflectivity must influence the shape of the melt pool. Eq. (16) is equivalent to Eq. (17) if $\sigma = 0.5$. The σ in this study was 1.0. The laser energy is more concentrated when the σ is smaller, which implies that the melt pool must be deeper when $\sigma < 1.0$. The simulations with different σ values will be performed in our future study.

On the other hand, Ren et al. have reported that the absorptivity obtained from the simulation using temperature-dependent reflectivity model, so-called Hagan–Ruben model was 0.404 (reflectivity: 0.596) and the effective absorptivity obtained from the calorimetric measurements was 0.424 (reflectivity: 0.576) under the condition of $P = 430$ W and $V = 0.6$ m/s. They have also reported that the time-averaged absorptivity was 0.094 (reflectivity: 0.906) for the simulation using the Fresnel reflection model, the form of which is slightly different from Eq. (15). According to Ren et al. [6], the Hagan-Ruben model is reasonable compared with the Fresnel model. Different reflectivity models and their values have been used in the previous studies and the value of the reflectivity significantly influences the melt pool dimensions obtained from the simulation.

The melt pool width: W increases slightly with increasing ϵ. The W obtained from the simulation does not agree with that obtained from the single-track experiment. The discrepancy may be caused by the effect of reflectivity perpendicular to the laser irradiation direction: around zero degrees of the laser incident angle. Fig. 10 shows that the reflectivity value varies significantly with ϵ. Since the laser irradiation direction is vertically downwards, the number of laser beams perpendicular to the laser direction should be extremely small. Although the reflectivity values vary significantly, the melt pool width in the horizontal direction was difficult to expand due to the small number of rays perpendicular to the laser direction. However, the melt pool width around the upper part of the substrate is often larger than that inside the melt pool. The larger W in the upper part may reflect the difference in melting behaviour between the powder bed and the substrate. To clarify the reason and to simulate the melt pool dimensions obtained from the single-track experiment, further studies for the simulations using constant reflectivity and the Hagen–Ruben model should be required.

4. Conclusions

In this study, a series of multi-physics CFD simulations were carried out to evaluate the influence of the parameters for the recoil pressure, the flow resistance force in the solid–liquid mushy zone and the Fresnel reflection model. The simulation results were quantitatively compared with the single-track experiments, and the following conclusions were drawn.

- The melt pool depth increased with increasing parameter α for the recoil pressure, while the melt pool width did not. The melt pool dimension obtained from the simulations with varying α did not agree with those obtained from the single-track experiment.
- The evaporated mass is converted to recoil pressure in the CFD algorithm. When the large α was used, the metal surface was deeply excavated and then the molten mass flowed backwards and accumulated. When the extremely low α, the molten metal mass hardly accumulated backwards; as a result, the powder bed and the upper part of the substrate disappeared after passing the laser.
- The melt pool depth and width were almost constant irrespective of the parameter C for the flow resistance force in the mushy zone, and did not agree with that obtained from the single-track experiment.
- The melt pool depth increased with increasing parameter ϵ in the Fresnel reflection model, while the melt pool width did not. The melt pool depth and width obtained from the simulations with varying ϵ did not agree with that obtained from the single track experiment.

The material used in this study is Inconel738LC; however, the melting and solidification behaviour of the metallic materials should be similar. Therefore, the results of this study will be applicable to the L-PBF for the metallic materials.

To produce a defect-free object using the L-PBF process, engineers should consider the effects of laser processing conditions (laser power, scan speed) and powder characteristics (particle size distribution, particle shape, packing homogeneity). It is quite difficult to optimise such processing parameters by experiment alone. In addition, the L-PBF process is capable of fabricating complex-shaped objects compared to the conventional fabrication processes. To take advantage of the features of L-PBF, it is essential to use computer-aided engineering (CAE) technologies, such as optimal design of the lattice structure, evaluation of residual stresses, defects and the microstructure to be formed. The multi-physics simulation is used in this study to evaluate defect formation. For such simulations to become a virtual testing tool, the melt pool dimensions should be reproduced by the simulation. In the light of the above discussion, the problems to be solved are as follows.

- To simulate a semicircular shape often observed in the experiment, not only the parameter tuning but also the solid particle dynamics such as coupling CFD and DEM and SPH should be incorporated to the simulation.
- The effect of microstructural parameters in the Kozeny–Carman equation, which is the basis of the Voller-Prakash model, should be evaluated. The flow resistance force model in the mushy zone should be extended for the inertial flow regime.
- The laser reflection model should include not only simple geometric reflection but also the temperature dependency.
- The standard deviation of the Gaussian distribution should be evaluated.

In this study, the processing parameter was a single condition: P = 300 W and V = 1.0 m/s. In order to verify the validity of the simulation, the authors have started a series of simulations where P and V are varied. The simulation results will be published elsewhere.

Not only the melt pool shape and defect formation, but also the microstructure is extremely important for the quality of the manufactured part. Pioneering work on the coupling of CFD with microstructure formation analysis, such as the phase field model [36] and the cellular automaton model [37], has been published in recent years. We will develop the coupling of CFD and microstructure formation model for microstructure control.

CRediT authorship contribution statement

Jun Katagiri: Conceptualization, Methodology, Validation, Formal analysis, Investigation, Data curation, Writing – original draft preparation, Writing – review & editing, visualization. **Masahiro Kusano:** Software, Validation, Formal analysis, Writing – review & editing. **Sukeharu Nomoto:** Methodology, Validation, Formal analysis, Writing – review & editing. **Makoto Watanabe:** Validation, Formal analysis, Writing – review & editing, Supervision, Project administration, Funding acquisition.

Declaration of competing interest

The authors declare no conflict of interest. The funders had no role in the design of the study; in the collection, analyses, or interpretation of data; in the writing of the manuscript; or in the decision to publish the results.

Data availability

The data that has been used is confidential

Acknowledgements

Financial support from the Council for Science, Technology, and Innovation (CSTI), Cross-ministerial Strategic Innovation Promotion Programme (SIP), “Materials Integration for revolutionary design system of structural materials” (Funding agency: JST) and Innovative Science and Technology Initiative for Security, Grant Number JPJ004596 implemented by the Acquisition, Technology, and Logistics Agency(ATLA)”.

References

[1] T. DebRoy, H.L. Wei, J.S. Zuback, T. Mukherjee, J.W. Elmer, J.O. Milewski, A.M. Beese, A. Wilson-Heid, A. De, W. Zhang, Additive manufacturing of metallic components – process, structure and properties, Prog. Mater. Sci. 92 (2018) 112–224, http://dx.doi.org/10.1016/j.pmatsci.2017.10.001.

[2] R. Seede, D. Shoukr, B. Zhang, A. Whitt, S. Gibbons, P. Flater, A. Elwany, R. Arroyave, I. Karaman, An ultra-high strength martensitic steel fabricated using selective laser melting additive manufacturing: Densification, microstructure, and mechanical properties, Acta Mater. 186 (2020) 199–214, http://dx.doi.org/10.1016/j.actamat.2019.12.037.

[3] D. Grange, A. Queva, G. Guillemot, M. Bellet, J.D. Bartout, C. Colin, Effect of processing parameters during the laser beam melting of Inconel 738: Comparison between simulated and experimental melt pool shape, J. Mater Process. Technol. 289 (2021) http://dx.doi.org/10.1016/j.jmatprotec.2020.116897.

[4] L. Wang, Y. Zhang, H.Y. Chia, W. Yan, Mechanism of keyhole pore formation in metal additive manufacturing, npj Comput. Mater. 8 (2022) http://dx.doi.org/10.1038/s41524-022-00699-6.

[5] M. Bayat, S. Mohanty, J.H. Hattel, Multiphysics modelling of lack of fusion voids formation and evolution in In718 made by multitrack/multi-layer L-PBF, Int. J. Heat Mass Transfer 139 (2019) 95–114, http://dx.doi.org/10.1016/j.ijheatmasstransfer.2019.05.003.

[6] Z. Ren, D.Z. Zhang, G. Fu, J. Jiang, M. Zhao, High-fidelity modelling of selective laser melting copper alloy: Laser reflection behavior and thermal-fluid dynamics, Mater. Des. 207 (2021) http://dx.doi.org/10.1016/j.matdes.2021.109857.

[7] P. Ninpetch, P. Kowitwarangkul, S. Mahathanabodee, P. Chalermkarnnon, P. Rattanadecho, Computational investigation of thermal behavior and molten metal flow with moving laser heat source for selective laser melting process, Case Stud. Therm. Eng. 24 (2021) http://dx.doi.org/10.1016/j.csite.2021.100860.

[8] W. Wang, W. Lin, R. Yang, Y. Wu, J. Li, Z. Zhang, Z. Zhai, Mesoscopic evolution of molten pool during selective laser melting of superalloy Inconel 738 at elevating preheating temperature, Mater. Des. 213 (2022) http://dx.doi.org/10.1016/j.matdes.2021.110355.

[9] S.I. Anisimov, Vaporization of metal absorbing laser radiation, J. Exp. Theor. Phys. 27 (1968) 182–183.

[10] A. Klassen, T. Scharowsky, C. Körner, Evaporation model for beam based additive manufacturing using free surface lattice Boltzmann methods, J. Phys. D: Appl. Phys. 47 (2014) http://dx.doi.org/10.1088/0022-3727/47/27/275303.

[11] V.R. Voller, C. Prakash, A fixed grid numerical modelling methodology for convection–diffusion mushy region phase-change problems, Int. J. Heat Mass Transfer 30 (1987) 1709–1719.

[12] J.H. Cho, S.J. Na, Implementation of real-time multiple reflection and fresnel absorption of laser beam in keyhole, J. Phys. D: Appl. Phys. 39 (2006) 5372–5378, http://dx.doi.org/10.1088/0022-3727/39/24/039.

[13] E. Li, Z. Zhou, L. Wang, H. Shen, R. Zou, A. Yu, Particle scale modelling of melt pool dynamics and pore formation in selective laser melting additive manufacturing, Powder Technol. 397 (2022) 117012, http://dx.doi.org/10.1016/j.powtec.2021.11.056.
[14] W. Alphonso, M. Baier, S. Carmignato, J. Hattel, M. Bayat, On the possibility of doing reduced order, thermo-fluid modelling of laser powder bed fusion (L-PBF) – assessment of the importance of recoil pressure and surface tension, J. Manuf. Process. 94 (2023) 564–577, http://dx.doi.org/10.1016/j.jmapro.2023.03.040.
[15] P.A. Cundall, O.D.L. Strack, A discrete element model for granular assemblies, Géotechnique 29 (1979) 47–65.
[16] H. Versteeg, W. Malalasekera, An Introduction to Computational Fluid Dynamics: The Finite Volume Method, Pearson Education Limited, 2007.
[17] H.G. Weller, G. Tabor, H. Jasak, C. Fureby, A tensorial approach to computational continuum mechanics using object-oriented techniques, Comput. Phys. 12 (6) (1998) 620–631, http://dx.doi.org/10.1063/1.168744.
[18] J.H. Ferziger, Computational Methods for Fluid Dynamics: J.H. Ferziger, M. Períc, Springer-Verlag, Berlin, 1996.
[19] T. Maríc, J. Höpken, K.G. Mooney, The OpenFOAM Technology Primer, Zenodo, 2021, http://dx.doi.org/10.5281/zenodo.4630596.
[20] L. Cao, Mesoscopic-scale simulation of pore evolution during laser powder bed fusion process, Comput. Mater. Sci. 179 (2020) http://dx.doi.org/10.1016/j.commatsci.2020.109686.
[21] M. Afrasiabi, C. Lüthi, M. Bambach, K. Wegener, Multi-resolution SPH simulation of a laser powder bed fusion additive manufacturing process, Appl. Sci. (Switzerland) 11 (2021) http://dx.doi.org/10.3390/app11072962.
[22] A. Queva, G. Guillemot, C. Moriconi, C. Metton, M. Bellet, Numerical study of the impact of vaporisation on melt pool dynamics in laser powder bed fusion - application to in718 and Ti–6Al–4V, Addit. Manuf. 35 (2020) http://dx.doi.org/10.1016/j.addma.2020.101249.
[23] J.-P. Fürstenau, H. Wessels, C. Weißenfels, P. Wriggers, Generating virtual process maps of SLM using powder-scale SPH simulations, Comput. Part. Mech. 7 (2020) 655–677, http://dx.doi.org/10.1007/s40571-019-00296-3.
[24] J. Katagiri, M. Kusano, S. Minamoto, H. Kitano, K. Daimaru, M. Tsujii, M. Watanabe, Melt pool shape evaluation by single-track experiments and finite-element thermal analysis: Balling and lack of fusion riteria for generating process window of inconel738lc, Materials 16 (2023) http://dx.doi.org/10.3390/ma16041729.
[25] L. Wang, Y. Zhang, W. Yan, Evaporation model for keyhole dynamics during additive manufacturing of metal, Phys. Rev. A 14 (2020) http://dx.doi.org/10.1103/PhysRevApplied.14.064039.
[26] R. Murayama, E. Ohmura, I. Miyamoto, H. Hara, N. Inoue, Thermohydrodynamics analysis on mechanism of bump formation in laser texturing, Q. J. Jpn. Weld. Soc. 18 (3) (2000) 373–380, http://dx.doi.org/10.2207/qjjws.18.373.
[27] H. Chen, W. Yan, Spattering and denudation in laser powder bed fusion process: Multiphase flow modelling, Acta Mater. 196 (2020) 154–167, http://dx.doi.org/10.1016/j.actamat.2020.06.033.
[28] B. Mahmoodi, S. Hosseini, G. Ahmadi, CFD–DEM simulation of a pseudo two-dimensional spouted bed comprising coarse particles, Particuology 43 (2019) 171–180, http://dx.doi.org/10.1016/j.partic.2017.12.014.
[29] I. Mema, J.T. Padding, Fluidization of elongated particles: effect of multi-particle correlations for drag, lift, and torque in CFD-DEM, AIChE J. 67 (5) (2021) e17157, http://dx.doi.org/10.1002/aic.17157.
[30] T. Yu, J. Zhao, Semi-coupled resolved CFD–DEM simulation of powder based selective laser melting for additive manufacturing, Comput. Methods Appl. Mech. Engrg. 377 (2021) http://dx.doi.org/10.1016/j.cma.2021.113707.
[31] T. Yu, J. Zhao, Quantitative simulation of selective laser melting of metals enabled by new high-fidelity multiphase, multiphysics computational tool, Comput. Methods Appl. Mech. Engrg. 399 (2022) http://dx.doi.org/10.1016/j.cma.2022.115422.
[32] S.L. Fuchs, P.M. Praegla, C.J. Cyron, W.A. Wall, C. Meier, A versatile SPH modeling framework for coupled microfluid-powder dynamics in additive manufacturing: binder jetting, material jetting, directed energy deposition and powder bed fusion, Eng. Comput. 38 (2022) 4853–4877, http://dx.doi.org/10.1007/s00366-022-01724-4.
[33] P.C. Carman, Fluid flow through granular beds, Trans. Inst. Chem. Eng. 15 (1937) 150–166.
[34] S. Whitaker, The Forchheimer equation: A theoretical development, Transp. Porous Media 25 (1996) 27–61, http://dx.doi.org/10.1007/BF00141261.
[35] S. Ergun, Fluid flow through packed columns, Chem. Eng. Prog. 48 (1952) 89–94, http://dx.doi.org/10.1029/JB088iS01p0B353.
[36] M. Yang, L. Wang, W. Yan, Phase-field modeling of grain evolutions in additive manufacturing from nucleation, growth, to coarsening, npj Comput. Mater. 7 (2021) http://dx.doi.org/10.1038/s41524-021-00524-6.
[37] Th. Camus, D. Maisonnette, O. Baulin, O. Senninger, G. Guillemot, Ch.-A. Gandin, Three-dimensional modeling of solidification grain structures generated by laser powder bed fusion, Materialia 30 (2023) 101804, http://dx.doi.org/10.1016/j.mtla.2023.101804.